

Crossover or First-Order: Impacts of Regularization

Xin-Peng Li  ^{1, 2, *} Hao-Ran Zhang  ^{1, 2} Zhu-Fang Cui  ^{1, 2, †} and Thomas Klähn  ^{3, ‡}

¹*School of Physics, Nanjing University, Nanjing, Jiangsu 210093, China*

²*Institute for Nonperturbative Physics, Nanjing University, Nanjing, Jiangsu 210093, China*

³*Department of Physics & Astronomy, California State University Long Beach, Long Beach, CA 90840, USA*

(Dated: December 18, 2025)

The equation of state of hot, dense nuclear matter plays a fundamental role in many areas. However, owing to the nonperturbative nature of strong interactions, a reliable treatment is still under debate. We use a symmetry-preserving treatment of a vector \otimes vector contact interaction to study related issues at nonzero temperature or quark chemical potential, and carefully compare a noncovariant and a covariant regularization scheme. The numerical results show that the character of the phase transition depends sensitively on the regularization scheme and parameter choices.

I. INTRODUCTION

The Standard Model of particle physics stands as the most successful theoretical framework in modern high-energy physics, having been subjected to and passed a wide range of experimental tests over the past several decades. It provides a unified description of three of the four known fundamental interactions in nature: electromagnetic, weak, and strong interactions. Among these, the strong interaction, which is described by the theory of quantum chromodynamics (QCD), is of particular importance. QCD is a non-Abelian gauge theory based on the $SU(3)_c$ color group, where quarks interact via the exchange of gluons. While perturbation theory has been proven to be extremely powerful at high energies, where the coupling constant becomes weak owing to asymptotic freedom, the situation changes dramatically at low energies. In the infrared regime, the QCD coupling grows large [1–5] and renders perturbative methods ineffective, thereby necessitating alternative nonperturbative approaches.

The thermodynamics of strongly interacting matter, encapsulated in the equation of state (EoS) of QCD, plays a fundamental role in both cosmology and astrophysics. In cosmology, the QCD EoS governs the dynamics of the early universe during the quark-hadron transition, possibly influencing the evolution of primordial fluctuations and thus potentially leaving observable imprints in the cosmic microwave background or relic abundances [6–8]. In astrophysics, it dictates the internal structure and stability of compact stellar objects, such as neutron stars and hybrid stars. Accurate knowledge of the EoS at high baryon density, or chemical potential (μ), is essential for determining properties such as maximum stellar masses, radii, and tidal deformabilities, which can now be constrained by multimesenger observations, including gravitational-wave detections from binary neutron star mergers [9, 10]. Thus, a quantitative and reliable

determination of the QCD phase structure and its corresponding EoS is a central challenge of modern theoretical physics.

Despite extensive progress achieved through lattice QCD simulations, serious limitations remain. At vanishing chemical potential, lattice QCD has provided quantitatively reliable results for the EoS, the pseudo-critical temperature of the crossover transition, and fluctuations of conserved charges. However, at nonzero μ , lattice methods are plagued by the sign problem that arises from the complex phase of the fermion determinant [11]. This makes straightforward Monte Carlo sampling impractical and severely restricts applicability in the low-temperature T , high- μ domain, precisely the regime of relevance for neutron star interiors and heavy-ion collisions at lower beam energies. While methods such as reweighting, Taylor expansions, or analytic continuation from imaginary chemical potential have been explored, none of them yield a fully controlled and systematically improvable approach at large μ [12, 13].

In light of these obstacles, a variety of effective models have been proposed to capture essential features of QCD in regimes inaccessible to lattice simulations. Among them, for example, the Nambu-Jona-Lasinio (NJL) model and its Polyakov-loop extended version (PNJL) have been widely employed to investigate chiral symmetry breaking, its restoration at nonzero T and μ , as well as qualitative aspects of the phase diagram. The NJL model successfully incorporates spontaneous chiral symmetry breaking and dynamical mass generation, which are hallmarks of low-energy QCD [14–29]. Nevertheless, it also has well-known shortcomings: the absence of confinement, dependence on ultraviolet cutoff schemes that violate Poincaré covariance, and a strong sensitivity of predictions to parameter choices and regularization prescriptions [30, 31]. As a result, while the NJL framework provides valuable intuition, its quantitative reliability remains questionable.

On the other hand, a popular first-principles continuum, nonperturbative approach that preserves fundamental symmetries is the Dyson-Schwinger equations (DSEs), which offer a system of coupled integral equations for Green's functions that are valid across all en-

* xpli@mail.nju.edu.cn

† phy cui@nju.edu.cn

‡ thomas.klaehn@csulb.edu

ergy scales [32–35]. In particular, DSEs respect Poincaré covariance and allow for the simultaneous study of confinement, dynamical chiral symmetry breaking, and their interrelation at zero T and μ . While truncations of the infinite tower of equations are unavoidable, systematic schemes such as the rainbow-ladder approximation and beyond have been proven capable of producing results consistent with both lattice QCD and experimental observations in many contexts; for example, Refs. [36–46].

In this work, we adopt a rainbow-truncated quark DSE with a local contact kernel to explore features of the QCD phase structure at nonzero (T, μ) . In this set of approximations, the bulk thermodynamics is practically mean-field equivalent to NJL-type models [40]. Crucially, because the contact interaction is nonrenormalizable, the regulator is part of the model. As we demonstrate, this leads to situations where the choice of the regularization scheme—not the interaction—drastically affects the behavior of matter under extreme conditions, and can determine whether the phase transition at low T is a crossover or first-order.

II. FRAMEWORK

A practical continuum approach to the strong interaction—providing a viable alternative to numerical simulations of lattice-regularized QCD—is offered by continuum Schwinger function methods (CSMs). These methods have been successfully applied to studies of QCD at finite temperature and chemical potential, offering direct access to the infrared behavior of correlation functions and the associated dynamical phenomena; see, e.g., Refs. [33, 34, 47, 48]. The present analysis is formulated within this framework. In preparation for the results that follow, we therefore begin by outlining the Dyson–Schwinger equations (DSEs) that form the basis of our calculation.

A. Quark DSE and order parameters

At nonzero temperature and chemical potential (T, μ) , the quark gap equation, or DSE for the dressed-quark propagator, can be written as (in Euclidean space) [32–35]

$$S^{-1}(\vec{p}, \tilde{\omega}_n) = i\vec{\gamma} \cdot \vec{p} + i\gamma_4 \tilde{\omega}_n + m + \Sigma(\vec{p}, \tilde{\omega}_n), \quad (1)$$

with self energy given by

$$\begin{aligned} \Sigma(\vec{p}, \tilde{\omega}_n) &= \int_{l,q} g^2 D_{\mu\nu}(\vec{p} - \vec{q}, \Omega_{nl}; T, \mu) \\ &\quad \times \gamma_\mu \frac{\lambda^a}{2} S(\vec{q}, \tilde{\omega}_l) \Gamma_\nu^a(\vec{p}, \tilde{\omega}_n, \vec{q}, \tilde{\omega}_l; T, \mu), \end{aligned} \quad (2)$$

where $\tilde{\omega}_n = \omega_n + i\mu$, $\omega_n = (2n + 1)\pi T$, with $n \in \mathbb{Z}$ the fermion Matsubara frequencies, m is the current quark

mass, $\int_{l,q} := T \sum_{l=-\infty}^{\infty} \int_{-\infty}^{\infty} \frac{d^3 q}{(2\pi)^3}$, $\Omega_{nl} = \tilde{\omega}_n - \tilde{\omega}_l = 2(n - l)\pi T$, and the dressed-quark propagator has the general form

$$S^{-1}(\vec{p}, \tilde{\omega}_n) = i\vec{\gamma} \cdot \vec{p} A(\vec{p}, \tilde{\omega}_n) + i\gamma_4 \tilde{\omega}_n C(\vec{p}, \tilde{\omega}_n) + B(\vec{p}, \tilde{\omega}_n). \quad (3)$$

The scalar functions, $F = A, B, C$, are complex and satisfy

$$F(\vec{p}, \tilde{\omega}_n)^* = F(\vec{p}, \tilde{\omega}_{-n-1}). \quad (4)$$

For the gluon propagator, a particularly simple and useful model is provided by the symmetry-preserving treatment of a contact (momentum-independent) vector \otimes vector quark-quark interaction (SCI) [49],

$$g^2 D_{\mu\nu} = \delta_{\mu\nu} \frac{4\pi\alpha_{ir}}{m_G^2}, \quad (5)$$

where α_{ir} is the zero-momentum value of the running-coupling constant [2–5, 50], and m_G is a gluon mass-scale that generated dynamically in QCD [1, 51, 52].

We can see that, akin with the Nambu–Jona–Lasinio model [14, 53], this interaction does not have momentum dependence, so that related equations are largely algebraic, and derivations and formulae become highly transparent, which makes the outcomes easy to interpret and even enables meaningful comparisons with results from more sophisticated interactions. The physical relevance of SCI results can also be appreciated under careful interpretation. Therefore, it is widely used in many topics; for example, Refs. [54–62].

With these treatments, and taking the implicitly associated “Rainbow approximation”, $\Gamma_\nu^a(\vec{p}, \tilde{\omega}_n, \vec{q}, \tilde{\omega}_l; T, \mu) = \frac{\lambda^a}{2} \gamma_\nu$, for the dressed quark-gluon vertex, the scalar functions satisfy,

$$A(\vec{p}, \tilde{\omega}_n) = 1, \quad (6a)$$

$$\begin{aligned} C(\vec{p}, \tilde{\omega}_n) &= 1 \\ &\quad + \frac{32\pi}{3\tilde{\omega}_n} \frac{\alpha_{ir}}{m_G^2} \int_{l,q} \frac{\tilde{\omega}_l C(\vec{q}, \tilde{\omega}_l)}{\vec{q}^2 + \tilde{\omega}_l^2 C^2(\vec{q}, \tilde{\omega}_l) + B^2(\vec{q}, \tilde{\omega}_l)}, \end{aligned} \quad (6b)$$

$$\begin{aligned} B(\vec{p}, \tilde{\omega}_n) &= m \\ &\quad + \frac{64\pi}{3} \frac{\alpha_{ir}}{m_G^2} \int_{l,q} \frac{B(\vec{q}, \tilde{\omega}_l)}{\vec{q}^2 + \tilde{\omega}_l^2 C^2(\vec{q}, \tilde{\omega}_l) + B^2(\vec{q}, \tilde{\omega}_l)}. \end{aligned} \quad (6c)$$

Since the integrand here is \vec{p} -momentum independent, while the sum is $\tilde{\omega}_n$ independent, a solution at one value of \vec{p} and $\tilde{\omega}_n$ is the solution at all values; viz., any nonzero solution must be of the form,

$$B(\vec{p}, \tilde{\omega}_n) =: R_B, \quad (7a)$$

$$\tilde{\omega}_n(C(\vec{p}, \tilde{\omega}_n) - 1) =: -iR_C, \quad (7b)$$

and Eq. (4) entails that R_B and R_C are real numbers. Then,

$$R_C = \frac{8}{3\pi} \frac{\alpha_{ir}}{m_G^2} \int_{n,s} s^{\frac{1}{2}} \frac{i\tilde{\omega}'_l}{s + \tilde{\omega}_n'^2 + R_B^2}, \quad (8a)$$

$$R_B = m + \frac{16}{3\pi} \frac{\alpha_{ir}}{m_G^2} R_B \int_{n,s} s^{\frac{1}{2}} \frac{1}{s + \tilde{\omega}_n'^2 + R_B^2}, \quad (8b)$$

where $\mu' = \mu - R_C$, $\tilde{\omega}_n' = \omega_n + i\mu'$; $s = \vec{q}^2$ and $\int_{n,s} := T \sum_{n=-\infty}^{\infty} \int_0^{\infty} ds$. We can see that mathematically R_C is always linked with μ , and plays a role in reducing it. Sometimes μ' is also referred to as the renormalized chemical potential [18].

Eq. (8) could also be written in an alternative form. Defining $E_{s,R_B} = \sqrt{s + R_B^2}$, one obtains

$$R_C = \frac{4}{3\pi} \frac{\alpha_{ir}}{m_G^2} \int_s s^{\frac{1}{2}} [n_+ - n_-], \quad (9a)$$

$$R_B = m + \frac{8}{3\pi} \frac{\alpha_{ir}}{m_G^2} R_B \int_s \frac{s^{\frac{1}{2}}}{E_{s,R_B}} [n_+ + n_-], \quad (9b)$$

where

$$\begin{aligned} n_{\pm} &= T \sum_{n=-\infty}^{\infty} \frac{1}{E_{s,R_B} \mp i\tilde{\omega}_n'} \\ &= T \sum_{n=-\infty}^{\infty} \frac{E_{s,R_B} \pm \mu'}{(E_{s,R_B} \pm \mu')^2 + \omega_n^2} \\ &= \frac{1}{2} - \frac{1}{1 + e^{\frac{1}{T}(E_{s,R_B} \pm \mu')}}. \end{aligned} \quad (10)$$

To provide a quantitative way to distinguish different phases, order parameters are usually defined in phase transition studies. The quark condensate (scalar density) is one order parameter for the chiral symmetry restoration transition, defined via the dressed-quark propagator [24, 63, 64],

$$\begin{aligned} \langle \bar{\psi} \psi \rangle &= -N_C \int_{n,q} \text{tr}_D S(\vec{q}, \tilde{\omega}_n) \\ &= -N_C \frac{3}{16\pi} \frac{m_G^2}{\alpha_{ir}} (R_B - m), \end{aligned} \quad (11)$$

where $N_C = 3$ is the quark color number. On the other hand, the total quark number density (vector density) is another popular order parameter [14, 65, 66], especially for nonzero μ areas,

$$\begin{aligned} \langle \psi^\dagger \psi \rangle &= \langle \bar{\psi} \gamma_4 \psi \rangle = -N_C \int_{n,q} \text{tr}_D \gamma_4 S(\vec{q}, \tilde{\omega}_n) \\ &= N_C \frac{3}{8\pi} \frac{m_G^2}{\alpha_{ir}} R_C. \end{aligned} \quad (12)$$

From Eq. (11) and Eq. (12), we can clearly see the physical meaning of R_B and R_C . R_B is usually called the effective quark mass, while R_C is closely related to quark number; hence, it is not surprising that R_C has the opposite effect to that of μ .

To highlight some of the similarities and differences with the formulation of the NJL model, we present the two sets of equations side by side for comparison.

Following the formulation of the NJL model in Ref. [18], the corresponding equations before regularization are

$$\begin{aligned} \mu' &= \mu - g_{NJL} \frac{N_f}{2\pi^2} \int_s s^{\frac{1}{2}} [n_+ - n_-] \\ &=: \mu - g'_{NJL} \int_s s^{\frac{1}{2}} [n_+ - n_-], \end{aligned} \quad (13a)$$

$$\begin{aligned} M &= m + G_{NJL} \frac{N_C N_f}{\pi^2} M \int_s \frac{s^{\frac{1}{2}}}{E_{s,M}} [n_+ + n_-] \\ &=: m + G'_{NJL} M \int_s \frac{s^{\frac{1}{2}}}{E_{s,M}} [n_+ + n_-], \end{aligned} \quad (13b)$$

where M is the constituent mass, g_{NJL} is the coupling constant of the four-fermion interaction, and

$$G_{NJL} = \frac{4N_C + 1}{4N_C} g_{NJL} \quad (14)$$

is a renormalized coupling constant introduced in Ref. [18]. One may now arrive at the following identity:

$$G'_{NJL} = \frac{1}{2}(4N_c + 1)g'_{NJL}. \quad (15)$$

Comparing Eq. (9) and Eq. (13), one sees that these expressions exhibit a strong formal resemblance to each other. However, they exhibit different N_c scaling. Indeed, defining the integral prefactors in Eq. (9) to be g_{SCI} , G_{SCI} , respectively, one has

$$G_{SCI} = 2g_{SCI}. \quad (16)$$

which should be contrasted with Eq. (15). This comparison reveals a qualitative difference between a standard NJL model treatment and the SCI insofar as couplings in the μ and M equations are concerned. SCI and NJL couplings evidently carry different color factors. This difference originates from the fact that, in the NJL framework, the effective four-fermion coupling is taken to be color singlet from the outset, so that octet channels are not explicitly retained when performing the Fierz rearrangement, whereas in the SCI formulation the underlying color-octet interaction is preserved and treated dynamically. At the physical value $N_c = 3$, however, couplings and cutoffs can be tuned so that, within the mean-field approximation for homogeneous matter, the two approaches are practically equivalent.

Additional significant differences emerge when one moves beyond the quark gap equation and examines, for instance, the Bethe-Salpeter equation for pseudoscalar mesons together with the associated elastic form factors. These quantities expose further discrepancies between the SCI and NJL constructions; see, e.g., Ref. [49] and citations thereof.

B. Regularization schemes

Analogously to the NJL model, the SCI is also non-renormalizable; therefore, a regularization scheme is unavoidable in working toward results with a meaningful

interpretation. Ideally, this regularization should maximally preserve the properties of the model and symmetries [14, 49, 65]. Currently, several schemes are available, each in some sense determines the model. For example, two of the most popular regularization schemes are the noncovariant but physically intuitive three-momentum (3M) cutoff regularization [14, 16, 18, 24, 26, 30, 31] and a covariant regularization in proper time (PT) form [14, 17, 19, 20, 28, 29, 36, 40, 49, 54–62]. Hereafter, we will compare them carefully.

1. Three-momentum cutoff regularization

This regularization does not take into account the contributions from momenta larger than a cutoff Λ_{3M} , i.e., integrates only within $s < \Lambda_{3M}^2$. Namely, the gap equation in Eq. (8) becomes

$$R_B = m + \frac{16}{3\pi} \frac{\alpha_{ir}}{m_G^2} R_B \int_{n,s}^{\Lambda_{3M}^2} s^{\frac{1}{2}} \frac{1}{s + \tilde{\omega}_n'^2 + R_B^2}. \quad (17)$$

2. Proper time regularization

The key treatment of this regularization is

$$\begin{aligned} \frac{1}{\mathcal{T}} &= \int_0^{+\infty} dx e^{-x\mathcal{T}} \rightarrow \int_{\tau_{uv}^2}^{\tau_{ir}^2} dx e^{-x\mathcal{T}} \\ &= \frac{1}{\mathcal{T}} \times e^{-x\mathcal{T}} \Big|_{x=\tau_{ir}^2}^{\tau_{uv}^2}, \text{ if } \mathcal{T} > 0, \end{aligned} \quad (18)$$

where $e^{-x\mathcal{T}} \Big|_{x=\tau_{ir}^2}^{\tau_{uv}^2} = e^{-\tau_{uv}^2\mathcal{T}} - e^{-\tau_{ir}^2\mathcal{T}}$ and $\tau_{uv} = \frac{1}{\Lambda_{uv}}$, $\tau_{ir} = \frac{1}{\Lambda_{ir}}$. Here, the ultraviolet cutoff Λ_{uv} plays a role like Λ_{3M} , but is much softer, while the infrared cutoff Λ_{ir} is introduced to mimic confinement.

For the nonzero μ case, $\mathcal{T} = s + \tilde{\omega}_n'^2 + R_B^2 = s + \omega_n^2 + R_B^2 - \mu'^2 + 2i\omega_n\mu'$ is a complex function and requires analytic continuation to the complex plane, so we rewrite Eq. (18) as

$$\begin{aligned} \frac{1}{\mathcal{T}} &= \int_0^{+\infty} dx e^{\mp x\mathcal{T}} \rightarrow \int_{\tau_{uv}^2}^{\tau_{ir}^2} dx e^{\mp x\mathcal{T}} = \frac{1}{\mathcal{T}} e^{\mp x\mathcal{T}} \Big|_{x=\tau_{uv}^2}^{\tau_{ir}^2} \\ &= \frac{1}{\mathcal{T}} e^{-\text{Sign}(\Re\mathcal{T})x\mathcal{T}} \Big|_{x=\tau_{uv}^2}^{\tau_{ir}^2} =: P(\mathcal{T}). \end{aligned} \quad (19)$$

where $\Re\mathcal{T}$ is the real part of \mathcal{T} and the symbol \pm here corresponds to the sign of $\Re\mathcal{T}$. There also exist some other complex forms of the PT regularization [30], in general, they have this form,

$$\begin{aligned} \frac{1}{\mathcal{T}} &= \frac{\mathcal{T}'}{\mathcal{T}} \times \frac{1}{\mathcal{T}'} = \frac{\mathcal{T}'}{\mathcal{T}} \int_0^{+\infty} dx e^{-x\mathcal{T}'} \\ &\rightarrow \frac{\mathcal{T}'}{\mathcal{T}} \int_{\tau_{uv}^2}^{\tau_{ir}^2} d\tau e^{-\tau\mathcal{T}'} = \frac{1}{\mathcal{T}} e^{-x\mathcal{T}'} \Big|_{x=\tau_{ir}^2}^{\tau_{uv}^2}, \end{aligned} \quad (20)$$

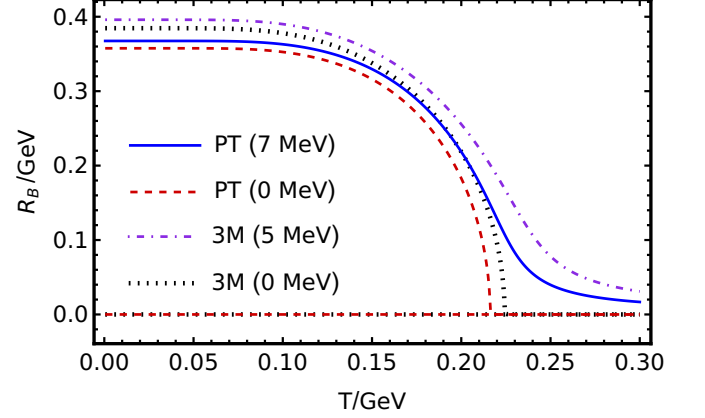


FIG. 1. Solutions of the gap equation at $\mu = 0$ GeV using PT (solid blue/dashed red curve for $m = 0.007/0$ GeV) and 3M (dot-dashed purple/dotted black curve for $m = 0.005/0$ GeV) regularizations.

where \mathcal{T}' only needs to satisfy $\Re\mathcal{T}' > 0$. One may also choose to rewrite Eq. (20) in many other reasonable forms, such as setting $\mathcal{T}' = |\mathcal{T}|$ or $\mathcal{T}' = i\mathcal{T}$ and so on. For example, we set $\mathcal{T}' = \text{Sign}(\Re\mathcal{T})\mathcal{T}$ in Eq. (19). However, we have checked that different forms mainly lead to some numerical differences in the results, instead of obvious qualitative changes. Considering the intrinsic discrepancy of this model with QCD, we choose to use Eq. (19) as an example for the following discussions.

III. IN MEDIUM ANALYSES

A. Zero chemical potential and nonzero temperature case

We begin by considering the zero μ and nonzero T case, which can help us understand the evolution of the early universe. In this case, many equations can be simplified; for example, $\tilde{\omega}_n = \omega_n$, $n_+ = n_-$, hence $R_C = 0$ GeV.

Turn to R_B , using the 3M regularization Eq. (17), Eq. (9) becomes

$$R_B = m + \frac{8}{3\pi} \frac{\alpha_{ir}}{m_G^2} R_B \int_0^{\Lambda_{3M}^2} \frac{s}{E_{s,R_B}} \tanh\left(\frac{E_{s,R_B}}{2T}\right) ds, \quad (21)$$

while using the PT regularization Eq. (19), Eq. (8) becomes [17, 36]

$$R_B = m + \frac{8}{3\sqrt{\pi}} \frac{\alpha_{ir}T}{m_G^2} R_B \int_{\tau_{uv}^2}^{\tau_{ir}^2} \frac{e^{-\tau R_B^2}}{\tau^{\frac{3}{2}}} \theta_2(e^{-4\pi^2 T^2 \tau}) d\tau, \quad (22)$$

where $\theta_2(q) = 2q^{\frac{1}{4}} \sum_{n=0}^{+\infty} q^{n(n+1)}$ is the Jacobi theta-function.

TABLE I. Regularization and interaction strength parameters used herein, whose values were chosen as described in the text. All quantities listed are measured in GeV, except for the coupling constant α_{ir} , which is dimensionless.

Schemes	m	α_{ir}	m_G	$\Lambda_{3M}/\Lambda_{uv}$	Λ_{ir}
3M	0.005	0.802π	0.8	0.650	-
PT	0.007	0.93π	0.8	0.905	0.24

B. Zero temperature and nonzero chemical potential case

Compact stars with their small ratio of temperature to chemical potential, $T/\mu \approx 0$, are well approximated by $T \rightarrow 0$ GeV and nonzero μ . In this case, the Matsubara frequencies become continuous, i.e., $\omega_n \rightarrow p_0$, and the sum then becomes an integral over the real axis,

$$\lim_{T \rightarrow 0} T \sum_{n=-\infty}^{\infty} f(\omega_n) = \frac{1}{2\pi} \int_{-\infty}^{\infty} dp_0 f(p_0), \quad (23)$$

so

$$R_C = \frac{4}{3\pi} \frac{\alpha_{ir}}{m_G^2} \int_0^{\max\{0, \mu'^2 - R_B^2\}} s^{\frac{1}{2}} ds$$

$$= \begin{cases} 0, & \mu' < R_B, \\ \frac{8}{9\pi} \frac{\alpha_{ir}}{m_G^2} (\mu'^2 - R_B^2)^{\frac{3}{2}}, & \mu' > R_B, \end{cases} \quad (24)$$

which gives the total quark number density as

$$\langle q^\dagger q \rangle = \begin{cases} 0, & \mu' < R_B, \\ N_C \frac{(\mu'^2 - R_B^2)^{\frac{3}{2}}}{3\pi^2}, & \mu' > R_B. \end{cases} \quad (25)$$

consistent with Ref. [67].

Turn to R_B , using Eq. (10) and the 3M regularization Eq. (17), Eq. (9) becomes

$$R_B = m + \frac{8}{3\pi} \frac{\alpha_{ir}}{m_G^2} R_B \int_{\max\{0, \mu'^2 - R_B^2\}}^{\Lambda_{3M}} \frac{s^{\frac{1}{2}}}{\sqrt{s + R_B^2}} ds, \quad (26)$$

while using the PT regularization Eq. (19), Eq. (8) becomes

$$R_B = m + \frac{8}{3\pi^2} \frac{\alpha_{ir}}{m_G^2} R_B \int_0^{\infty} ds \int_{-\infty}^{\infty} dp_0 s^{\frac{1}{2}} P(\mathcal{T}), \quad (27)$$

where $\mathcal{T} = s + p_0'^2 + R_B^2$ and $p_0' = p_0 + i\mu'$, hence $\Re \mathcal{T} = s + R_B^2 + p_0'^2 - \mu'^2$.

IV. RESULTS

We solve the gap equations using the parameters in Table I. These values are chosen in order to draw close comparison with NJL results. We set $\alpha_{ir} = 0.802\pi$ for the

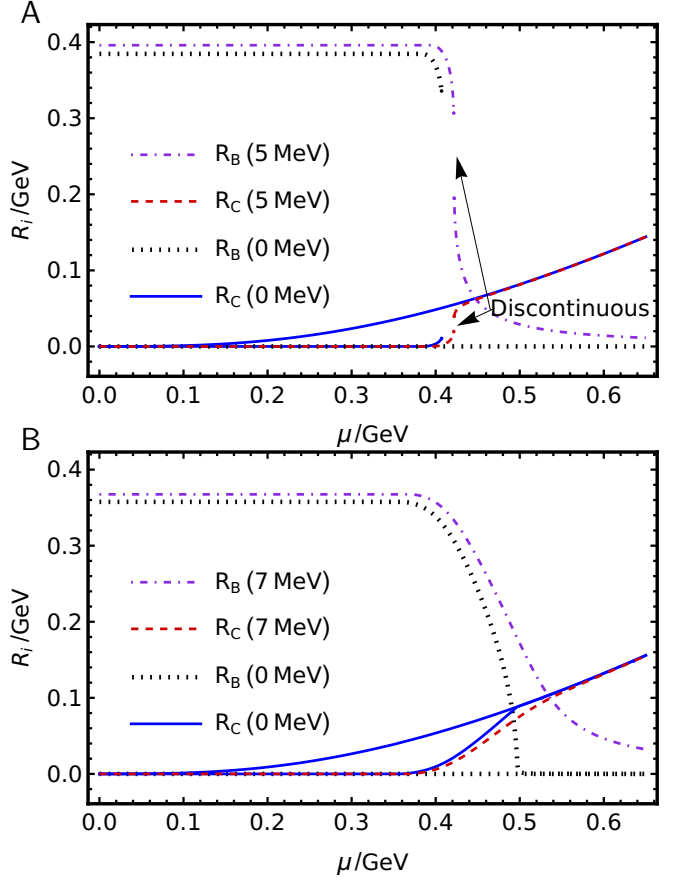


FIG. 2. Solutions of the gap equation with different regularization schemes at $T \rightarrow 0$ GeV. Panel A. 3M regularization; Panel B. PT regularization. Both: the dot-dashed purple and dashed red curves show R_B and R_C beyond the chiral limit, respectively, while the dotted black and solid blue curves represent the corresponding results in the chiral limit $m = 0$ GeV.

3M regularization used in Ref. [18] with $N_C = 3, N_f = 2$ so that $G_{SCI} = G_{NJL} \approx 5.5 \text{ GeV}^{-2}$ and then slightly retune Λ_{3M} from 0.631 GeV to 0.65 GeV to compensate for the coefficient mismatch between Eq. (15) and Eq. (16), thereby obtaining results analogous to those of the NJL results. PT parameters are fixed analogously to reproduce the correct vacuum solution, ensuring that in-medium differences reflect the impact of different regularization schemes rather than parameter tuning in vacuum.

Solutions of the gap equation with different regularization schemes are shown in Fig. 1 and Fig. 2, respectively.

We can see clearly from Fig. 1 that, in the chiral limit $m = 0$ GeV case, the gap equation always has a solution with restored chiral symmetry, i.e. $R_B = 0$ GeV, which is usually named the Wigner solution; see, e.g., [20, 24, 68]. Another solution is the chiral symmetry broken Nambu solution, i.e. $R_B \neq 0$ GeV. In domains where the Nambu and Wigner solutions coexist, the thermodynamically stable branch is the one that minimizes the thermodynamic potential. At low temperature this

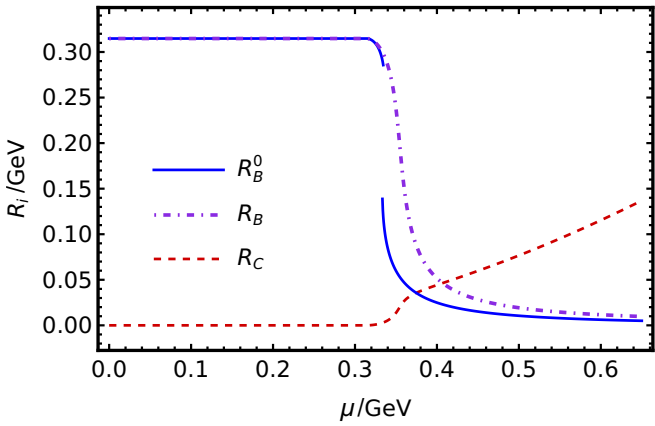


FIG. 3. R_C effect on the phase transition in the 3M regularization scheme. Legend: solid blue curve - ignore the effects of R_C using parameters from Table I and set $\alpha_{ir} = 0.73\pi$; dotdashed purple curve - the result of R_B restoring the effects of R_C ; dashed red curve - the result of R_C .

is the Nambu solution. Increasing the temperature, the system undergoes a second-order phase transition to the Wigner phase. [24, 34, 36] However, once we go beyond the chiral limit, there is only the Nambu solution, and the transition becomes a crossover, which has been discussed widely in the literature [36, 69–72]. Moreover, it is interesting to note that 3M and PT regularization schemes give very similar results, both qualitatively and quantitatively.

Next, we consider the $T \rightarrow 0$ GeV case, as shown in Fig. 2. In the 3M regularization, as shown in Fig. 2A, we can clearly see that there is a first-order phase transition. When going beyond the chiral limit, the Nambu and Wigner solutions coexist in the region from $\mu \approx 421.5$ MeV to $\mu \approx 422.0$ MeV. For the PT regularization scheme, the picture changes significantly. As shown in Fig. 2B, the pattern is almost the same as that in Fig. 1, besides R_C becoming nonzero and increasing gradually with μ . Namely, in this scheme, the μ effect is very similar to the T one. From Fig. 2, we also notice that $R_C = 0$ GeV is a good approximation at low μ ; while when μ is large, R_C effect is not negligible.

Comparing Fig. 1 and Fig. 2, we find that the qualitative effect of increasing T at zero μ is similar for both schemes, whereas with increasing μ at low T the regularization scheme determines the order of the phase transition.

V. DISCUSSION

To clearly show the influence of the vector mean field R_C , we use the 3M parameters from Table I and set $\alpha_{ir} = 0.73\pi$. As shown in Fig. 3, this turns the previously observed first order phase transition from Fig. 2A into a crossover. If we set $R_C = 0$ GeV, the curve will move to lower μ and turn first-order again. Obviously,

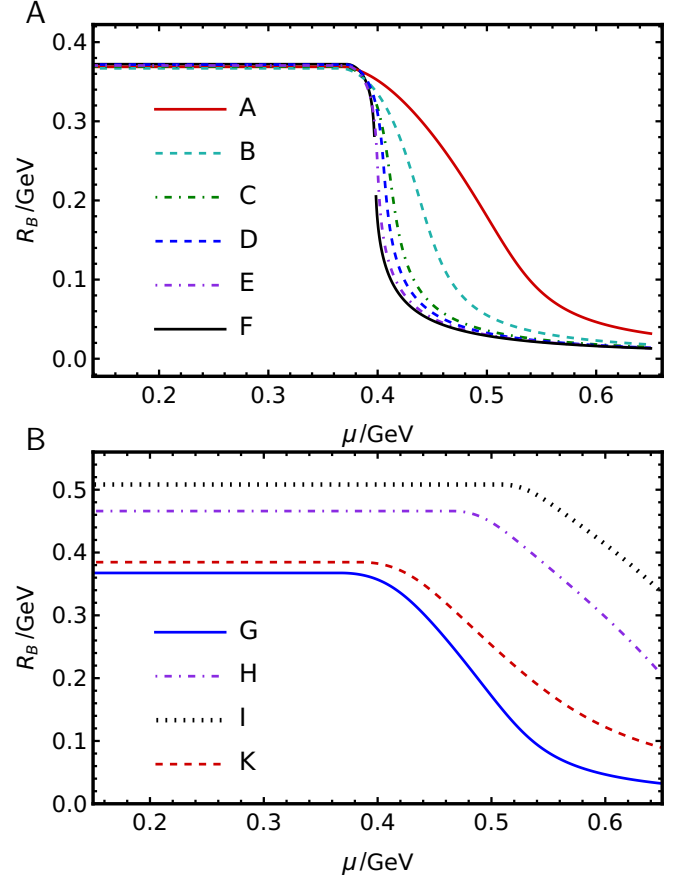


FIG. 4. Comparison of solutions for different parameter sets. Panel A. Using 6 different parameters listed in the upper panel of Table II. Panel B. Using 4 different parameters listed in the lower panel of Table II.

this shows that R_C has a significant impact on the order of the phase transition and weakens the first order phase transition.

The key point originates from the minus sign in the effective chemical potential $\mu' = \mu - R_C$, which reflects the repulsive nature of the vector interaction among quarks [14, 73]. Since $R_C \propto \langle \psi^\dagger \psi \rangle$ grows with the quark number density, the repulsion increases as the system becomes denser. Consequently, achieving a further increase in density requires a larger external chemical potential to compensate for this enhanced internal repulsion. In other words, R_C systematically suppresses the influence of the chemical potential on the thermodynamic potential. This mechanism naturally leads to a weakening of the first-order chiral phase transition at high density.

Next, we analyze how the regularization schemes change the order of the phase transition. As mentioned above, since both models are nonrenormalizable, one has to introduce some special treatment to cure the ultraviolet divergence and make the quantities finite. Comparing Eq. (26) and Eq. (27), we find that the 3M regularization scheme imposes a hard cutoff Λ_{3M}^2 which eliminates contributions from higher momenta. Contrarily, the momentum integration goes up to $+\infty$ in the PT regulariza-

TABLE II. Parameter sets used in Fig. 4. Upper panel - 6 sets of Λ_{uv} and Λ_H for Eq. (28). Lower panel - 4 parameter sets for PT regularization. All quantities listed except for the dimensionless coupling constant α_{ir} are measured in GeV.

Cases	Λ_{uv}	Λ_H	α_{ir}	m
A	0.905	10	0.73π	0.005
B	1.5	0.787	0.73π	0.005
C	3	0.67	0.73π	0.005
D	5	0.64	0.73π	0.005
E	10	0.62	0.73π	0.005
F	100	0.605	0.73π	0.005
G	0.905	-	0.93π	0.007
H	0.905	-	1.15π	0.007
I	1	-	0.93π	0.007
K	0.905	-	0.93π	0.02

tion, with a soft cutoff due to the exponential damping factor $e^{-\tau^2\mathcal{T}}$.

To interpolate between hard cutoff and the soft exponential damping factor, we introduce the following equation,

$$R_B = m + \frac{8}{3\pi^2} \frac{\alpha_{ir}}{m_G^2} R_B \int_0^{\Lambda_H^2} ds \int_{-\infty}^{\infty} dp_0 s^{\frac{1}{2}} P(\mathcal{T}), \quad (28)$$

where $\mathcal{T} = s + p_0'^2 + R_B^2$. The exponential factor related to τ_{ir} is approximately zero; we ignore it for this discussion. Using the PT parametrization from Table I we vary Λ_{uv} as shown in Table II. In order to keep the vacuum mass $R_B(T = \mu = 0 \text{ GeV})$ constant for all Λ_{uv} we adjust Λ_H accordingly. In this way we interpolate from a PT type solution (A) to a 3M type solution (F). Fig. 4A shows how at $T = 0 \text{ GeV}$ the PT crossover in $R_B(\mu)$ then gradually changes into a first order phase transition.

We conclude that, as a noncovariant regularization scheme, the 3M cutoff treatment introduces a hard and sharp cutoff in momentum space, which tends to result in more abrupt changes in the behaviors of the physical quantities (we use effective mass as an example, and the similar pattern appears in related quantities), expressed as a first-order phase transition. While the PT regularization is a covariant scheme that smoothly regularizes the interaction by introducing an exponential damping factor, which is gentle and soft, so that most related quantities and processes will also tend to change continuously, expressed as a crossover.

Finally, we discuss the influence of the remaining parameters on the phase transition as listed in the lower panel of Table II. The results are shown in Fig. 4B. With PT regularization, any combination of Λ_{uv} , α_{ir} and m results in a crossover phase transition at $T \rightarrow 0 \text{ GeV}$; for the 3M regularization, we show numerically that the dimensionless quantity

$$\chi := \frac{\alpha_{ir} \Lambda_{3M}^2}{m_G^2} \quad (29)$$

determines the order of the phase transition. Fig. 5 shows

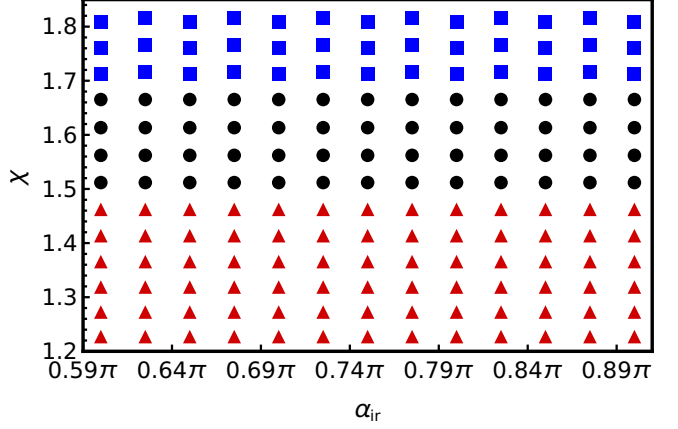


FIG. 5. The size of the dimensionless parameter χ , Eq. (29), controls the order of the transition at $m = 0.005 \text{ GeV}$. Legend: blue squares – first-order for both $R_C = 0 \text{ GeV}$ and $R_C \neq 0 \text{ GeV}$; black circles – first-order only at $R_C = 0 \text{ GeV}$ and crossover at $R_C \neq 0 \text{ GeV}$; red triangles – crossover in both cases.

that smaller values of $\chi \lesssim 1.7$ lead to a crossover at $m = 0.005 \text{ GeV}$, whereas $\chi \gtrsim 1.7$ produce a first-order transition. Although one may set $R_C = 0 \text{ GeV}$, its effect is merely to shift the numerical value of χ down without altering this qualitative behavior.

VI. CONCLUSIONS

We used a contact interaction to compare the effects of different regularization schemes: the noncovariant three-momentum cutoff and the covariant proper time treatment, at nonzero temperature T or chemical potential μ . At zero μ and nonzero T , the chiral phase transition is a smooth crossover for both regularization schemes. When turning to the low T and nonzero μ region, different regularization schemes and parametrizations may provide qualitatively distinct behavior, namely, crossover or first-order. We find that different parameter choices produce only quantitative changes in the covariant regularization, yet they determine the order of the phase transition in the noncovariant case.

This sensitivity is problematic. In a renormalizable quantum field theory, the phase structure is expected to be independent of the regularization procedure if it has been carried out consistently. In this study, we kept vacuum observables and the underlying interaction fixed. In conclusion, for the non-renormalizable contact model the regulator is effectively part of the physics, and predictions concerning the phase structure in medium are intrinsically scheme dependent.

At the same time, the bare-vertex approximation violates the Ward identity at nonzero chemical potential, indicating that adopting something like Ball–Chiu vertex is a natural step for future refinement.

ACKNOWLEDGMENTS

We thank C. D. Roberts for valuable suggestions. Work supported by: Natural Science Foundation of

Jiangsu Province, grant no. BK20220122; National Natural Science Foundation of China, grant no. 12233002.

[1] D. Binosi, C. Mezrag, J. Papavassiliou, C. D. Roberts, and J. Rodriguez-Quintero, Process-independent strong running coupling, *Phys. Rev. D* **96**, 054026 (2017), arXiv:1612.04835 [nucl-th].

[2] Z.-F. Cui, J.-L. Zhang, D. Binosi, F. de Soto, C. Mezrag, J. Papavassiliou, C. D. Roberts, J. Rodríguez-Quintero, J. Segovia, and S. Zafeiropoulos, Effective charge from lattice QCD, *Chin. Phys. C* **44**, 083102 (2020), arXiv:1912.08232 [hep-ph].

[3] D. d'Enterria *et al.*, The strong coupling constant: state of the art and the decade ahead, *J. Phys. G* **51**, 090501 (2024), arXiv:2203.08271 [hep-ph].

[4] A. Deur, V. Burkert, J. P. Chen, and W. Korsch, Experimental determination of the QCD effective charge $\alpha_{g_1}(Q)$, *Particles* **5**, 171 (2022), arXiv:2205.01169 [hep-ph].

[5] A. Deur, S. J. Brodsky, and C. D. Roberts, QCD running couplings and effective charges, *Prog. Part. Nucl. Phys.* **134**, 104081 (2024), arXiv:2303.00723 [hep-ph].

[6] E. Witten, Cosmic separation of phases, *Phys. Rev. D* **30**, 272 (1984).

[7] J. H. Applegate and C. J. Hogan, Relics of Cosmic Quark Condensation, *Phys. Rev. D* **31**, 3037 (1985).

[8] C. Schmid, D. J. Schwarz, and P. Widerin, Peaks above the Harrison-Zel'dovich spectrum due to the quark-gluon to hadron transition, *Phys. Rev. Lett.* **78**, 791 (1997), arXiv:astro-ph/9606125.

[9] E. Annala, T. Gorda, A. Kurkela, and A. Vuorinen, Gravitational-wave constraints on the neutron-star-matter Equation of State, *Phys. Rev. Lett.* **120**, 172703 (2018), arXiv:1711.02644 [astro-ph.HE].

[10] C. A. Raithel, Constraints on the Neutron Star Equation of State from GW170817, *Eur. Phys. J. A* **55**, 80 (2019), arXiv:1904.10002 [astro-ph.HE].

[11] O. Philipsen, The QCD equation of state from the lattice, *Prog. Part. Nucl. Phys.* **70**, 55 (2013), arXiv:1207.5999 [hep-lat].

[12] P. de Forcrand, Simulating QCD at finite density, *PoS LAT2009*, 010 (2009), arXiv:1005.0539 [hep-lat].

[13] K. Nagata, Finite-density lattice QCD and sign problem: Current status and open problems, *Prog. Part. Nucl. Phys.* **127**, 103991 (2022), arXiv:2108.12423 [hep-lat].

[14] S. P. Klevansky, The nambu-jona-lasinio model of quantum chromodynamics, *Rev. Mod. Phys.* **64**, 649 (1992).

[15] T. Klähn, R. Lastowiecki, and D. B. Blaschke, Implications of the measurement of pulsars with two solar masses for quark matter in compact stars and heavy-ion collisions: A Nambu-Jona-Lasinio model case study, *Phys. Rev. D* **88**, 085001 (2013), arXiv:1307.6996 [nucl-th].

[16] X.-y. Xin, S.-x. Qin, and Y.-x. Liu, Improvement on the Polyakov-Nambu-Jona-Lasinio model and the QCD phase transitions, *Phys. Rev. D* **89**, 094012 (2014).

[17] Z.-F. Cui, Y.-L. Du, and H.-S. Zong, The two-flavor NJL model with two-cutoff proper time regularization, *Int. J. Mod. Phys. Conf. Ser.* **29**, 1460232 (2014).

[18] Y. Lu, Y.-L. Du, Z.-F. Cui, and H.-S. Zong, Critical behaviors near the (tri-)critical end point of QCD within the NJL model, *Eur. Phys. J. C* **75**, 495 (2015), arXiv:1508.00651 [hep-ph].

[19] S. Shi, Y.-C. Yang, Y.-H. Xia, Z.-F. Cui, X.-J. Liu, and H.-S. Zong, Dynamical chiral symmetry breaking in the NJL model with a constant external magnetic field, *Phys. Rev. D* **91**, 036006 (2015), arXiv:1503.00452 [hep-ph].

[20] Q.-W. Wang, Z.-F. Cui, and H.-S. Zong, Studies of Wigner-Weyl solution and external magnetic field in an NJL model, *Phys. Rev. D* **94**, 096003 (2016).

[21] K.-I. Aoki, S.-I. Kumamoto, and M. Yamada, Phase structure of NJL model with weak renormalization group, *Nucl. Phys. B* **931**, 105 (2018), arXiv:1705.03273 [hep-th].

[22] G.-y. Shao, Z.-d. Tang, X.-y. Gao, and W.-b. He, Baryon number fluctuations and the phase structure in the PNJL model, *Eur. Phys. J. C* **78**, 138 (2018), arXiv:1708.04888 [hep-ph].

[23] T. G. Khunjua, K. G. Klimenko, and R. N. Zhokhov, Chiral imbalanced hot and dense quark matter: NJL analysis at the physical point and comparison with lattice QCD, *Eur. Phys. J. C* **79**, 151 (2019), arXiv:1812.00772 [hep-ph].

[24] Z.-F. Cui, S.-S. Xu, B.-L. Li, A. Sun, J.-B. Zhang, and H.-S. Zong, Wigner solution of the quark gap equation, *Eur. Phys. J. C* **78**, 770 (2018), arXiv:1804.06594 [hep-ph].

[25] L. M. Abreu, E. B. S. Corrêa, C. A. Linhares, and A. P. C. Malbouisson, Finite-volume and magnetic effects on the phase structure of the three-flavor Nambu-Jona-Lasinio model, *Phys. Rev. D* **99**, 076001 (2019), arXiv:1903.09249 [hep-ph].

[26] C.-X. Cui, J.-Y. Li, S. Matsuzaki, M. Kawaguchi, and A. Tomiya, New Aspect of Chiral SU(2) and U(1) Axial Breaking in QCD, *Particles* **7**, 237 (2024), arXiv:2205.12479 [hep-ph].

[27] A. E. B. Pasqualotto, R. L. S. Farias, W. R. Tavares, S. S. Avancini, and G. Krein, Causality violation and the speed of sound of hot and dense quark matter in the Nambu-Jona-Lasinio model, *Phys. Rev. D* **107**, 096017 (2023), arXiv:2301.10721 [hep-ph].

[28] J.-L. Zhang and J. Wu, Pion-photon and kaon-photon transition distribution amplitudes in the Nambu-Jona-Lasinio model, *Chin. Phys. C* **48**, 083106 (2024), arXiv:2402.12757 [hep-ph].

[29] G. Gifari, P. T. P. Hutařuk, and T. Mart, Nuclear medium meson structures from the Schwinger proper-time Nambu-Jona-Lasinio model, *Phys. Rev. D* **110**, 014043 (2024), arXiv:2402.19048 [hep-ph].

[30] H. Kohyama, D. Kimura, and T. Inagaki, Regularization dependence on phase diagram in Nambu-Jona-Lasinio model, *Nucl. Phys. B* **896**, 682 (2015), arXiv:1501.00449 [hep-ph].

[31] H. Kohyama, D. Kimura, and T. Inagaki, Parameter

fitting in three-flavor Nambu–Jona-Lasinio model with various regularizations, *Nucl. Phys. B* **906**, 524 (2016), arXiv:1601.02411 [hep-ph].

[32] C. D. Roberts and A. G. Williams, Dyson-Schwinger equations and their application to hadronic physics, *Prog. Part. Nucl. Phys.* **33**, 477 (1994), arXiv:hep-ph/9403224.

[33] C. S. Fischer, Infrared properties of QCD from Dyson-Schwinger equations, *J. Phys. G* **32**, R253 (2006), arXiv:hep-ph/0605173.

[34] C. D. Roberts and S. M. Schmidt, Dyson-Schwinger equations: Density, temperature and continuum strong QCD, *Prog. Part. Nucl. Phys.* **45**, S1 (2000), arXiv:nucl-th/0005064.

[35] C. S. Fischer, QCD at finite temperature and chemical potential from Dyson-Schwinger equations, *Prog. Part. Nucl. Phys.* **105**, 1 (2019), arXiv:1810.12938 [hep-ph].

[36] K.-l. Wang, Y.-x. Liu, L. Chang, C. D. Roberts, and S. M. Schmidt, Baryon and meson screening masses, *Phys. Rev. D* **87**, 074038 (2013).

[37] A.-M. Zhao, Z.-F. Cui, Y. Jiang, and H.-S. Zong, Non-linear susceptibilities under the framework of Dyson-Schwinger equations, *Phys. Rev. D* **90**, 114031 (2014), arXiv:1412.6884 [hep-ph].

[38] B. Wang, Y.-L. Wang, Z.-F. Cui, and H.-S. Zong, Effect of the chiral chemical potential on the position of the critical endpoint, *Phys. Rev. D* **91**, 034017 (2015).

[39] S.-S. Xu, Z.-F. Cui, B. Wang, Y.-M. Shi, Y.-C. Yang, and H.-S. Zong, Chiral phase transition with a chiral chemical potential in the framework of Dyson-Schwinger equations, *Phys. Rev. D* **91**, 056003 (2015), arXiv:1505.00316 [hep-ph].

[40] T. Klahn and T. Fischer, Vector interaction enhanced bag model for astrophysical applications, *Astrophys. J.* **810**, 134 (2015), arXiv:1503.07442 [nucl-th].

[41] Z.-F. Cui, I. C. Cloet, Y. Lu, C. D. Roberts, S. M. Schmidt, S.-S. Xu, and H.-S. Zong, Critical endpoint in the presence of a chiral chemical potential, *Phys. Rev. D* **94**, 071503 (2016), arXiv:1604.08454 [nucl-th].

[42] F. Gao and Y.-x. Liu, QCD phase transitions via a refined truncation of Dyson-Schwinger equations, *Phys. Rev. D* **94**, 076009 (2016), arXiv:1607.01675 [hep-ph].

[43] B.-L. Li, Z.-F. Cui, B.-W. Zhou, S. An, L.-P. Zhang, and H.-S. Zong, Finite volume effects on the chiral phase transition from Dyson-Schwinger equations of QCD, *Nucl. Phys. B* **938**, 298 (2019), arXiv:1711.04914 [hep-ph].

[44] P. Isserstedt, M. Buballa, C. S. Fischer, and P. J. Gunkel, Baryon number fluctuations in the QCD phase diagram from Dyson-Schwinger equations, *Phys. Rev. D* **100**, 074011 (2019), arXiv:1906.11644 [hep-ph].

[45] K. Raya, A. Bashir, and P. Roig, Contribution of neutral pseudoscalar mesons to a_μ^{HLL} within a Schwinger-Dyson equations approach to QCD, *Phys. Rev. D* **101**, 074021 (2020), arXiv:1910.05960 [hep-ph].

[46] T. Klaehn, L. C. Loveridge, and M. Cierniak, Chaos in QCD? Gap equations and their fractal properties, *Particles* **6**, 470 (2023).

[47] J. M. Pawłowski, Aspects of the functional renormalisation group, *Annals Phys.* **322**, 2831 (2007), arXiv:hep-th/0512261.

[48] C. Chen, F. Gao, and S.-x. Qin, Screening masses of positive- and negative-parity hadron ground states, including those with strangeness, *Phys. Rev. D* **112**, 014022 (2025), arXiv:2412.15045 [hep-ph].

[49] L. X. Gutierrez-Guerrero, A. Bashir, I. C. Cloet, and C. D. Roberts, Pion form factor from a contact interaction, *Phys. Rev. C* **81**, 065202 (2010), arXiv:1002.1968 [nucl-th].

[50] D. Binosi, Emergent Hadron Mass in Strong Dynamics, *Few Body Syst.* **63**, 42 (2022), arXiv:2203.00942 [hep-ph].

[51] M. Ding, C. D. Roberts, and S. M. Schmidt, Emergence of Hadron Mass and Structure, *Particles* **6**, 57 (2023), arXiv:2211.07763 [hep-ph].

[52] M. N. Ferreira and J. Papavassiliou, Gauge Sector Dynamics in QCD, *Particles* **6**, 312 (2023), arXiv:2301.02314 [hep-ph].

[53] M. Oertel, M. Hempel, T. Klähn, and S. Typel, Equations of state for supernovae and compact stars, *Rev. Mod. Phys.* **89**, 015007 (2017), arXiv:1610.03361 [astro-ph.HE].

[54] A. Ahmad and A. Raya, Inverse magnetic catalysis and confinement within a contact interaction model for quarks, *J. Phys. G* **43**, 065002 (2016), arXiv:1602.06448 [hep-ph].

[55] Z.-F. Cui, J.-L. Zhang, and H.-S. Zong, Proper time regularization and the QCD chiral phase transition, *Sci. Rep.* **7**, 45937 (2017).

[56] J.-L. Zhang, Z.-F. Cui, J. Ping, and C. D. Roberts, Contact interaction analysis of pion GTMDs, *Eur. Phys. J. C* **81**, 6 (2021), arXiv:2009.11384 [hep-ph].

[57] P.-L. Yin, Z.-F. Cui, C. D. Roberts, and J. Segovia, Masses of positive- and negative-parity hadron ground-states, including those with heavy quarks, *Eur. Phys. J. C* **81**, 327 (2021), arXiv:2102.12568 [hep-ph].

[58] P. Cheng, F. E. Serna, Z.-Q. Yao, C. Chen, Z.-F. Cui, and C. D. Roberts, Contact interaction analysis of octet baryon axial-vector and pseudoscalar form factors, *Phys. Rev. D* **106**, 054031 (2022), arXiv:2207.13811 [hep-ph].

[59] B. A. Zamora, E. C. Martínez, J. Segovia, and J. J. Cobos-Martínez, Contact interaction model for the η and η' mesons in a Schwinger-Dyson-Bethe-Salpeter approach to QCD: Masses, decay widths, and transition form factors, *Phys. Rev. D* **107**, 114031 (2023), arXiv:2304.14887 [hep-ph].

[60] Y. Yu, P. Cheng, H.-Y. Xing, F. Gao, and C. D. Roberts, Contact interaction study of proton parton distributions, *Eur. Phys. J. C* **84**, 739 (2024), arXiv:2402.06095 [hep-ph].

[61] G. Paredes-Torres, L. X. Gutierrez-Guerrero, A. Bashir, and Á. S. Miramontes, First radial excitations of mesons and diquarks in a contact interaction, *Phys. Rev. D* **109**, 114006 (2024), arXiv:2405.06101 [hep-ph].

[62] D.-D. Cheng, Z.-F. Cui, M. Ding, C. D. Roberts, and S. M. Schmidt, Pion Boer–Mulders function using a contact interaction, *Eur. Phys. J. C* **85**, 115 (2025), arXiv:2409.11568 [hep-ph].

[63] S. J. Brodsky, C. D. Roberts, R. Shrock, and P. C. Tandy, Confinement contains condensates, *Phys. Rev. C* **85**, 065202 (2012), arXiv:1202.2376 [nucl-th].

[64] F. Gao, J. Chen, Y.-X. Liu, S.-X. Qin, C. D. Roberts, and S. M. Schmidt, Phase diagram and thermal properties of strong-interaction matter, *Phys. Rev. D* **93**, 094019 (2016), arXiv:1507.00875 [nucl-th].

[65] R. L. S. Farias, G. Dallabona, G. Krein, and O. A. Battistel, Extension of the Nambu-Jona-Lasinio model at high densities and temperatures using an implicit regularization scheme, *Phys. Rev. C* **77**, 065201 (2008), arXiv:hep-

ph/0604203.

[66] H. Chen, W. Yuan, L. Chang, Y.-X. Liu, T. Klahn, and C. D. Roberts, Chemical potential and the gap equation, *Phys. Rev. D* **78**, 116015 (2008), arXiv:0807.2755 [nucl-th].

[67] A. M. Halasz, A. D. Jackson, R. E. Shrock, M. A. Stephanov, and J. J. M. Verbaarschot, On the phase diagram of qcd, *Phys. Rev. D* **58**, 096007 (1998), arXiv:hep-ph/9804290.

[68] S.-x. Qin, L. Chang, H. Chen, Y.-x. Liu, and C. D. Roberts, Phase diagram and critical endpoint for strongly-interacting quarks, *Phys. Rev. Lett.* **106**, 172301 (2011), arXiv:1011.2876 [nucl-th].

[69] Y. Aoki, G. Endrodi, Z. Fodor, S. D. Katz, and K. K. Szabo, The Order of the quantum chromodynamics transition predicted by the standard model of particle physics, *Nature* **443**, 675 (2006), arXiv:hep-lat/0611014.

[70] A. Bazavov *et al.*, The chiral and deconfinement aspects of the QCD transition, *Phys. Rev. D* **85**, 054503 (2012), arXiv:1111.1710 [hep-lat].

[71] K. Fukushima and T. Hatsuda, The phase diagram of dense QCD, *Rept. Prog. Phys.* **74**, 014001 (2011), arXiv:1005.4814 [hep-ph].

[72] T. Bhattacharya *et al.*, QCD Phase Transition with Chiral Quarks and Physical Quark Masses, *Phys. Rev. Lett.* **113**, 082001 (2014), arXiv:1402.5175 [hep-lat].

[73] M. Buballa, NJL model analysis of quark matter at large density, *Phys. Rept.* **407**, 205 (2005), arXiv:hep-ph/0402234.